Biomacromolecules

Article

Cite This: Biomacromolecules 2018, 19, 3970−3982

pubs.acs.org/Biomac

A Hierarchical Model To Understand the Processing of Polysaccharides/Protein-Based Films in Ionic Liquids

Amnah Hadadi,[†] John W. Whittaker,[‡,§] David E. Verrill,[†] Xiao Hu,[∥] Luca Larini,*[,‡,§] and David Salas-de la Cruz*[,†,§]

[†]Department of Chemistry, [‡]Department of Physics, and [§]Center for Computational and Integrative Biology, Rutgers University-Camden, Camden, New Jersey 08102, United States

[∥]Department of Physics and Astronomy, Department of Biomedical Engineering, Rowan University, Glassboro, New Jersey 08028, United States

Supporting Information

ABSTRACT: In recent years, biomaterials from abundant and renewable sources have shown potential in medicine and materials science alike. In this study, we combine theoretical modeling, molecular dynamics simulations, and several experimental techniques to understand the regeneration of cellulose/silk-, chitin/silk-, and chitosan/silk-based biocomposites after dissolution in ionic liquid and regeneration in water. We propose a novel theoretical model that correlates the composite's microscopic structure to its bulk properties. We rely on modeling non-cross-linked biopolymers that present layer-like structures such as β-sheets and we successfully predict structural, thermal, and mechanical properties of a mixture of these biomolecules. Our model and experiments show that the solubility of the pure substance in the chosen solvent can be used to modulate the amount of crystallinity of the biopolymer blend, as measured by attenuated total reflectance Fourier transform infrared spectroscopy (ATR-FTIR). Thermogravimetric analysis (TGA) shows that the decomposition temperature of the blended biocomposites compared to their pure counterparts is reduced in accordance with our theoretical predictions. The morphology of the material is further characterized through scanning electron microscopy (SEM) and shows differently exposed surface area depending on the blend. Finally, differential scanning calorimetry (DSC) is performed to characterize the residual water content in the material, essential for explaining the regeneration process in water. As a final test of the model, we compare our model's prediction of the Young's modulus with existing data in the literature. The model correctly reproduces experimental trends observed in the Young's modulus due to varying the concentration of silk in the biopolymer blend.

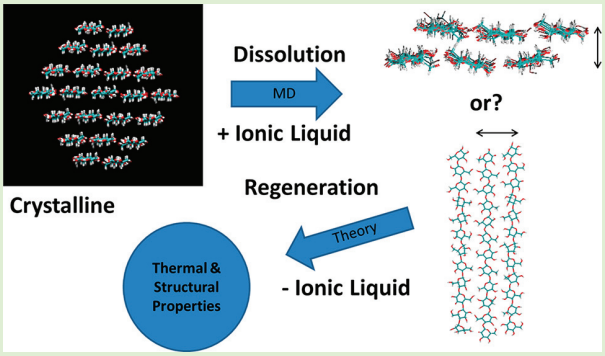

INTRODUCTION

Biomaterials are a rapidly expanding class of materials and have been of interest in recent decades due to their abundance, low cost, biocompatibility, and tunable morphological and physical properties.[1−5] These materials have been broadly used for the development of membranes and fibers for liquid and gas separation[6] and sensing,[7] fabrication of scaffolds for cartilage and bone regeneration,[8−10] and the creation of nanostructures for drug delivery.[11] The study of biomaterials includes aspects of medicine, biology, chemistry, engineering, environmental science, and materials science.

While biomaterials can, in principle, revolutionize modern materials science, there are still many open questions regarding their processability and our ability to predict their properties, especially of materials made from multiple biopolymer components. Transforming natural resources from their native state to a more usable form is nontrivial, being the subject of intense scientific scrutiny,[12−15] and immense effort has been put into understanding how the processing of a biomaterial affects its properties. Furthermore, the characterization, modulation, and application of biopolymers in the development of biomaterials is still a relatively recent development,[16] and the ever-growing catalogue of potential uses and methodologies[17−21] represents a considerable hurdle in the effort to anticipate and model a material's traits from first principles. Thus, this diverse field would benefit from a generalized, transferable approach that allows one to predict trends that can aid in more targeted designs of novel materials for special applications. The development of such an approach is a major aim of this study.

The analytical model presented here has its roots in the theory of coarse-graining. Examples of successful coarse-grained models are those in fluid dynamics[22] and polymer science,[23−25] as well as the theory of liquid crystals.[26]

Received: June 10, 2018
Revised: August 18, 2018
Published: August 21, 2018

DOI: 10.1021/acs.biomac.8b00903
Biomacromolecules 2018, 19, 3970−3982

Importantly, all of these models rely on the assumption that a detailed description of the molecular interactions of a *specific* material can be disregarded in lieu of a more general description that can be applied to a *class* of materials. In this way, we do not expect to predict the exact behavior of a material, but to predict trends that are common to a specific class of materials.

Here, we focus on modeling the merging of polysaccharides (e.g., cellulose, chitin) and protein (e.g., silk) into useful biocomposites and comparing this model with concrete experimental examples. Typically, these biopolymers are processed by dissolution (and purification) followed by a regenerative phase, and generally, the solvent adopted is different in each of these stages. In the study presented here, we use ionic liquid and water for the dissolution and regeneration processes, respectively. Ionic liquids (ILs) are an excellent alternative solvent and are used to dissolve natural polymers, offering the ability to tune the processability of a material.[27−34] They are characterized as green solvents since they are nonvolatile, nonflammable, and recyclable.[35] In addition to being green solvents, ILs have gained popularity due to their attractive chemical properties such as thermal stability, high ionic conductivity, negligible vapor pressure, and ease of recovery.[29] These solvents are salts, made up of a cationic and anionic component. The cationic species is responsible for certain chemical characteristics including the melting temperature and organic solubility, while the anionic species is responsible for the IL's air and water stability.[36] ILs are classified by their cationic group which falls into one of the following: (1) alkylammonium-, (2) dialkylimidazolium-, (3) phosphonium-, and (4) *N*-alkylpyridinium. Cationic groups such as 1-allyl-3-methylimidazolium (AMIM), 1-butyl-3-methylimidazolium (BMIM), and 1-ethyl-3-methylimidazolium (EMIM), and anionic groups such as chloride, bromide, acetate, or formate have been reported as the most effective solvents for cellulose, chitin, and silk.[30,37−45] These imidazolium cation solvents differ from each other by the substitution of a unique side chain at position C-1. The popularity of using the imidazolium ring as cation in ILs is due to its ease of synthesis, its low viscosity, its stability within oxidative/reductive conditions, its unique properties as a catalyst, and its chemoselectivity for a variety of organic reactions.[35]

Biomaterials are generally not used in their pure form and usually they are mixed with other biomaterials (permitting they are miscible), forming polymer blends. Polymer blends very often present morphologies that are different from that of the original material, which in turn leads to modified properties.[46] An example of this has been presented by Jin et al.[47] with respect to mixtures of silk and chitin. The author showed that when silk is added to the mixture, the protein intercalates between the chitin molecules. The change in structure alters the Young's modulus, which presents a sharp increase when a modest amount of silk is introduced to the system. Our group has previously analyzed the association of a protein (*Bombyx mori* mulberry silk fibroin or *Thai* silk fibroin) with a polysaccharide (Avicel microcrystalline cellulose) and assessed the spatiotemporal structure of the resulting biopolymer as a function of concentration and as a function of ionic liquid type.[38−40]

In the present study, our experiments focus on the mixture of cellulose, chitin, or chitosan with *Bombyx mori* silk. Silk has been shown to exhibit good mixing properties with polysaccharides.[29,47−49] Silk has other advantages such as strong (and dutifully characterized) mechanical properties, oxygen and water vapor permeability, biocompatibility, and biodegradability.[50−52] While in a regenerated state (often composed of predominantly random coil conformations) silk is brittle,[53] its properties can be ameliorated when mixed with other biopolymers and coagulation agents.[47,54−57]

This study is organized in the following fashion. First, we propose and derive a simple analytical model that allows us to garner information that describes connections between the arrangements of biopolymer mixtures and their structural and thermal properties. Further, we examine results from experiments that aim to characterize specific properties of polysaccharide/protein mixtures (blended after dissolution in ionic liquid) in order to compare our generalized theoretical predictions with those derived from concrete examples. Our theory correctly predicts trends observed in the crystallinity and thermal stability of biomaterials. Results from molecular dynamics simulations are also discussed and are used to further expand the scope of our predictions with respect to bridging the dissolution/regeneration process of biopolymers and the resulting material's characteristics. Finally, we conclude with predictions and discussion of the mechanical properties of regenerated biopolymer mixtures, namely, their Young's modulus, which is consistent with experimental data from previous published work.

MATERIAL AND METHODS

Material. *Bombyx mori* silk cocoons were purchased from Treenway Silks (Lakewood, CO). In order to remove the sericin coated on the silk fibers, silkworm cocoons were boiled in a 0.02 M $NaHCO_3$ (Sigma-Aldrich, USA) solution for 15 min, and then rinsed thoroughly with deionized water three times to remove sericin completely. The degummed silks were air-dried overnight, and put into a vacuum oven (30 inHg) at room temperature to remove the moisture on their surface. Avicel microcrystalline cellulose (Techware: Z26578−0) was acquired from Analtech. Chitin from shrimp shells was purchased from Sigma (C7170) and Chitosan was purchased from Sigma (448877). Before use, cellulose, chitin, and chitosan powder was placed under a vacuum oven at a temperature of 70 °C for 24 h. 1-Allyl-3-methylimidazolium chloride (98%) (AMIMCl) ionic liquid was purchased from Alfa Aesar. The ionic liquid was pretreated by being placed in vacuum oven (30 inHg) at 70 °C for 24 h, to ensure that water was removed from the solvent.

We have chosen several mixtures of polysaccharide and silk as listed in Table 1. All mixtures have been dissolve using the ionic liquid AMIMCl. It is important to note that, of course, different biomolecules do have a different solubility in different ionic liquids.[28,58,59] For instance, cellulose tends to dissolve more easily in AMIMCl when compared with chitin and chitosan, maybe as a consequence of a small but favorable van der Waals energy contribution between the sugar and cations (imidazolium ring).[60]

Table 1. Protein/Polysaccharide Samples Characterized in This Study

Polysaccharide	Silk	Abbreviations
	Cellulose	
80%	20%	CES20
20%	80%	CES80
	Chitin	
80%	20%	CHS20
20%	80%	CHS80
	Chitosan	
80%	20%	CTS20
20%	80%	CTS80

DOI: 10.1021/acs.biomac.8b00903
Biomacromolecules 2018, 19, 3970−3982

Sample Preparation. AMIMCl was placed in a test tube (approximately 95% w/w). Then the tube was placed on a hot plate. Solid pieces of α-chitin, chitosan, cellulose, or silk were added individually (about 5% w/w) until dissolved. The dissolution of the biopolymers was conducted at 103 °C ± 2 °C for 48 h using magnetic stirring. After 48 h, the dissolved biopolymer in ionic liquid solution was transferred between two glass slides. The glass slide were place in a Petri dish and 30 mL of water was added to coagulate the biopolymers. During coagulation the solution turned into solid films. After 48 h, the water was removed and solid film was dried in vacuum oven for 24 h at 50 °C. Finally, the solid films were stored in a desiccator chamber until characterization.

Attenuated Total Reflectance Fourier Transform Infrared spectroscopy (ATR-FTIR). Fourier transform infrared spectra (FTIR) analysis was performed using Bruker ALPHA-Platinum FTIR Spectrometer, with Platinum-Diamond sample module using Bruker OPUS Mentor Plus software version 7.2, Build: 7.2.139.1294. The spectra were collected in the wavenumber between 400 and 4000 cm^{-1}, resolution 4 cm^{-1}, 32 sample scans, and 128 background scans. Six locations were analyzed for each sample and averaged together. The percentage of the crystallinity of β-sheets within silk was obtained from each sample by selecting the Fourier self-deconvolution, and the frequency range was set between 1700 and 1500 cm^{-1} to enable the spectrum to be interactive in the selected wavenumber.[61] The parameters were set as follows: noise reduction 0.30 and bandwidth 25 using a Lorentzian, local least square, and Gauss shaped methods. To obtain the crystallinity of β-sheet, the sum numbers of β-sheet were divided by the sum numbers of the integral.

Thermogravimetric Analysis (TGA). Thermal data was obtained using thermogravimetric analysis (TGA) which was carried out on TA Instruments Discovery system, performed on all samples in a nitrogen atmosphere. The heating process was run at 10 °C/min ramp to 650 °C for average sample of 6 mg. Decomposition temperatures are defined as the maximum of the derivative of weight loss with respect to temperature.

Scanning Electron Microscope (SEM). The SEM images were taken on the LEO1450EP SEM at Rutgers University Camden campus. A small piece was mounted on carbon tape on Denton Desk II Au−Pd sputter coater. The samples were sputter coated and run in a light-vacuum of 10 V for 60 s. The magnification used in this paper is a scale bar of 2000× (10.00 μm).

Differential Scanning Calorimetry (DSC). Samples (approximately 5 mg) were enclosed in TZero aluminum pans and run in a TA Instruments Discovery with a refrigerated cooling system (RCS) and with nitrogen gas flow (25 mL min^{-1}). The standard aluminum reference was used to calibrate the heat capacity. Samples heated from 5 °C/min up to 120 °C to allow the water to evaporate. They were then cooled down to −30 °C, and heated up again to 170 °C.

Simulation Details. Cellulose molecules were built using the GAG Builder by GLYCAM[62] and assembled into layers using VMD,[63] while imidazolium-based chloride ionic liquid was built and parametrized using Antechamber[64] and GAFF.[65] All simulations were conducted using GROMACS 5.1.4[66−72] and parameters from the GLYCAM06[73] force field and GAFF were utilized throughout all simulations. Short-range nonbonded interactions were cut off at 1.2 nm, while long-range Coulombic interactions were calculated using the Particle Mesh Ewald method.[74,75] Long-range dispersion corrections were applied to energy and pressure. Periodic boundary conditions were applied in all directions for all simulations.

Starting structures of each system were first solvated with cation and neutralized with chloride counterions, then subjected to steepest descents energy minimization. NPT and NVT ensemble equilibrations, in that order, were then carried out on each system with position restraints applied to each heavy atom making up the D-glucose units. NPT equilibration time to constant density varied depending on the system. Temperature was maintained using a Berendsen weakly coupled thermostat[76] set to a reference temperature of 363.15 K with a time constant of 0.1 ps^{-1}. Pressure was also maintained isotropically using a weakly coupled barostat at 1 bar with a time constant of 1 ps^{-1} and center-of-mass position restraint reference coordinate scaling. NVT equilibration simulations were then performed with velocities generated according to a Maxwell distribution at T = 363.15 K and temperatures maintained using the same method as the NPT portion for 1 ns.

Following this final equilibration, production simulations began from these conformations. These simulations follow the same protocol as before, except that the Berendsen thermostat is replaced with the Nosé−Hoover thermostat.[77,78] Umbrella sampling[79] was performed on two separate cellulose systems: a two-layer configuration composed of 6 individual strands of cellulose (3 strands per layer) (Figure S1, panel A) and a single layer of 3 cellulose strands (Figure S1, panel B).

The pulling protocol was different for each system. In the case of the double layer, the goal was to separate the two layers from each other as if one was pulling two sheets of paper stacked on top of one another apart while also making an effort to keep the pieces of paper as flat as possible. To do this, we restrained the lower layer as described for equilibration but removed restraints from the top layer. From here, the free top layer was held fixed (0.0 nm ps^{-1} pull rate, spring constant of 10^5 kJ mol^{-1} nm^{-2}), subject to an umbrella potential, at varying distances d (Figure S1, panel A) away from the bottom layer using a combination of three-cylinder geometry groups with radii equaling about 1/6th of the length of the long axis of the layer. In order to further ensure the unrestrained layer remained flat with respect to the fixed reference layer, a series of fixed-distance pull groups (spring constant of 10^6 kJ mol^{-1} nm^{-2}) across the width of the layer were implemented. This was only to keep the layer as "taut" as possible; any information from these pulls was not used for analysis. Simulations were initially performed in increments of 0.25 Å in the y direction from the near-equilibrium center of mass (COM) separation between bottom and top layer of approximately 0.5 to 1.35 nm. Inspection of the resulting data revealed that in certain adjacent sampling windows, the respective COM separations along the y-coordinate did not overlap adequately, and thus, halfway between these windows, an extra simulation window was added to fill this gap (e.g., if position data from 0.50 and 0.525 nm COM separation did not overlap, a third window fixed at 0.5125 nm was performed). Eventually, sampling windows were also added at an increment of 0.20 Å from 0.44 to 0.48 nm COM distance in order to emphasize the energy minimum of ∼0.50 nm. This spacing culminated in 46 windows—each 200 ns—resulting in ∼9.2 μs of total simulation time.

In the case of the single layer, the goal was to "pluck" a chain from the edge of the layer and thus, a more routine protocol was implemented. Of the three chains that compose the layer, two were frozen (Figure S1, panel B) using the same position restraints mentioned previously. Five reference COM groups were assigned to oxygen atoms in closest proximity to five COM groups on the free, pulled chain which were located on glycosidic oxygens along the chain's axis from end to end. Along the z coordinate connecting these paired groups, the edge chain was held fixed (0.0 nm ps^{-1} pull rate, 10^6 kJ mol^{-1} nm^{-2} spring constant) at COM separation distances ranging from 0.40 to 2.00 nm with a sampling window spacing of 0.125 Å. Eventually, spacing of 0.2 Å was employed from 1.5 to 2.0 Å as at this point, these windows were sufficient for sampling. This spacing culminated in 114 windows, again each totaling 200 ns, resulting in ∼22.8 μs of total simulation time. Analysis was performed using the weighted histogram analysis method[79] (WHAM) as implemented in GROMACS 5.1.4.

THEORETICAL MODEL

In this section, we will propose a model that is able to predict observed experimental behavior presented in a later section. We will start by assuming that the crystalline form is composed of a set of layers stacked on each other (see Figure 1). It should be noted that the term "layer" is used in a very broad sense and we do not make any assumptions about the nature of the layer itself. For instance, each strand may represent the backbone of a single polymer, a section of a polymer, an entire β-sheet, or

DOI: 10.1021/acs.biomac.8b00903
Biomacromolecules 2018, 19, 3970−3982

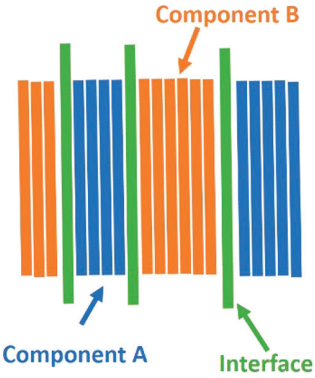

Figure 1. Schematic of an idealized local crystalline structure for a protein−polysaccharide blend. We assume that locally the material is composed of crystal chunks of component A (e.g., protein) and component B (e.g., polysaccharide) separated by interaction surfaces. The model describes the entropy of this system as the number of possible ways the interfaces can be arranged.

even a short fibril (though the latter is probably unlikely in most cases). The exact nature of the interaction between different molecules at the interfaces (whether they are hydrogen bonds, nonbonded interactions, etc.) is also considered very generally. Thanks to this generality, the model can be employed to study mixtures of molecules that belong to different chemical groups, such as proteins and sugars. As a consequence, the model is useful to determine whether the material under examination is composed of alternating disposition of "blocks" with uniform properties or not. While this may not necessarily represent every possible material, we will show that it is consistent with the polymer blends studied in this work. We will look further into this assumption in the simulations discussed later on.

Stacking Model. We expect that the cohesive energy will depend on the ability of each layer to properly adhere to the next layer. It is reasonable to expect that naturally occurring materials have evolved to maximize this property. If we assume that the system is a binary mixture of species A and B, this predicts that the cohesive energy ϵ_A for an A−A interface and ϵ_B for an B−B interface is much larger that the energy ϵ_{AB} for the interface A−B. Under these conditions, let us assume that the system is composed of N_A layers of component A, N_B layers of component B, and N_{AB} interfaces between components A and B. As each interface is composed of one layer of A and one layer of B, the layers that can form contiguous A and B sections of the crystals are $N'_A = N_A - N_{AB}$ and $N'_B = N_B - N_{AB}$. Based on these considerations, we now aim to find the configuration of layers that minimizes the free energy F of the system. The free energy F is defined as

$$F = E - TS \tag{1}$$

where E is the internal energy, T the temperature, and S the entropy. The energy of the system is written as

$$E = \left(N'_A + \frac{N_{AB}}{2}\right)\epsilon_A + \left(N'_B + \frac{N_{AB}}{2}\right)\epsilon_B + N_{AB}\epsilon_{AB} \tag{2}$$

$$E = \left(N_A - \frac{N_{AB}}{2}\right)\epsilon_A + \left(N_A - \frac{N_{AB}}{2}\right)\epsilon_B + N_{AB}\epsilon_{AB} \tag{3}$$

To compute the entropy, we will use the same strategy adopted for computing the specific heat of a group of harmonic oscillators (namely the Einstein model for the specific heat of a crystal). In this approach, we think of these interfaces as the delimiters of each energy level. The number of "quanta of energy" in each level is now replaced by the number of layers. In addition, each species can only occupy half of the available levels. With this in mind, we can write the entropy as

$$S_x/k_B = \left(N'_x + \frac{N_{AB}}{2}\right)\ln\left(N'_x + \frac{N_{AB}}{2}\right) - N_x'\ln N'_x - \frac{N_{AB}}{2}\ln\frac{N_{AB}}{2} \tag{4}$$

$$S_x/k_B = \left(N_x - \frac{N_{AB}}{2}\right)\ln\left(N_x - \frac{N_{AB}}{2}\right) - (N_x - N_{AB})\ln(N_x - N_{AB}) - \frac{N_{AB}}{2}\ln\frac{N_{AB}}{2} \tag{5}$$

where x stands for either A or B and k_B is the Boltzmann constant. Finally

$$F = \left(N_A - \frac{N_{AB}}{2}\right)\epsilon_A + \left(N_B - \frac{N_{AB}}{2}\right)\epsilon_B + N_{AB}\epsilon_{AB} - k_BT[S_A + S_B] \tag{6}$$

To find the equilibrium structure, we need the minimum of the free energy:

$$\frac{\partial F}{\partial N_{AB}} = -\frac{1}{2}(\epsilon_A + \epsilon_B - 2\epsilon_{AB}) - k_BT\left[-\frac{1}{2}\ln\left(N_A - \frac{N_{AB}}{2}\right) - \frac{1}{2}\ln\left(N_B - \frac{N_{AB}}{2}\right) + \ln(N_A - N_{AB}) + \ln(N_B - N_{AB}) - \ln\frac{N_{AB}}{2}\right] \tag{7}$$

Assuming that N_{AB} is smaller than N_A and N_B

$$\frac{\partial F}{\partial N_{AB}} \approx -\frac{1}{2}(\epsilon_A + \epsilon_B - 2\epsilon_{AB}) - k_BT\left[-\frac{1}{2}\ln(N_A) - \frac{1}{2}\ln(N_B) + \ln(N_A) + \ln(N_B) - \ln\frac{N_{AB}}{2}\right] \tag{8}$$

$$\frac{\partial F}{\partial N_{AB}} \approx -\frac{1}{2}(\epsilon_A + \epsilon_B - 2\epsilon_{AB}) - k_BT\left[\frac{1}{2}\ln(N_A) + \frac{1}{2}\ln(N_B) - \ln\frac{N_{AB}}{2}\right] \tag{9}$$

$$\frac{\partial F}{\partial N_{AB}} \approx -\frac{1}{2}(\epsilon_A + \epsilon_B - 2\epsilon_{AB}) - \frac{1}{2}k_BT\left[\ln\left(2\frac{N_AN_B}{N_{AB}^2}\right)\right] \tag{10}$$

The minimum is found for

$$\frac{\partial F}{\partial N_{AB}} \approx -\frac{1}{2}(\epsilon_A + \epsilon_B - 2\epsilon_{AB}) - \frac{1}{2}k_BT\left[\ln\left(2\frac{N_AN_B}{N_{AB}^2}\right)\right] = 0 \tag{11}$$

$$\frac{N_AN_B}{N_{AB}^2} = \frac{1}{2}\exp\left(-\frac{\epsilon_A + \epsilon_B - 2\epsilon_{AB}}{k_BT}\right) \tag{12}$$

To assess the validity of the model, we can make some reasonable guesses about the values of the parameters needed. We know that species A and B form crystals; thus, their energies ϵ_A and ϵ_B must be negative. In addition, we can guess that ϵ_{AB} is negative (otherwise the surface will not form) and smaller than the other energies because an A−B layer does not come together as favorably as an A−A or B−B layer. Thus:

DOI: 10.1021/acs.biomac.8b00903
Biomacromolecules 2018, 19, 3970−3982

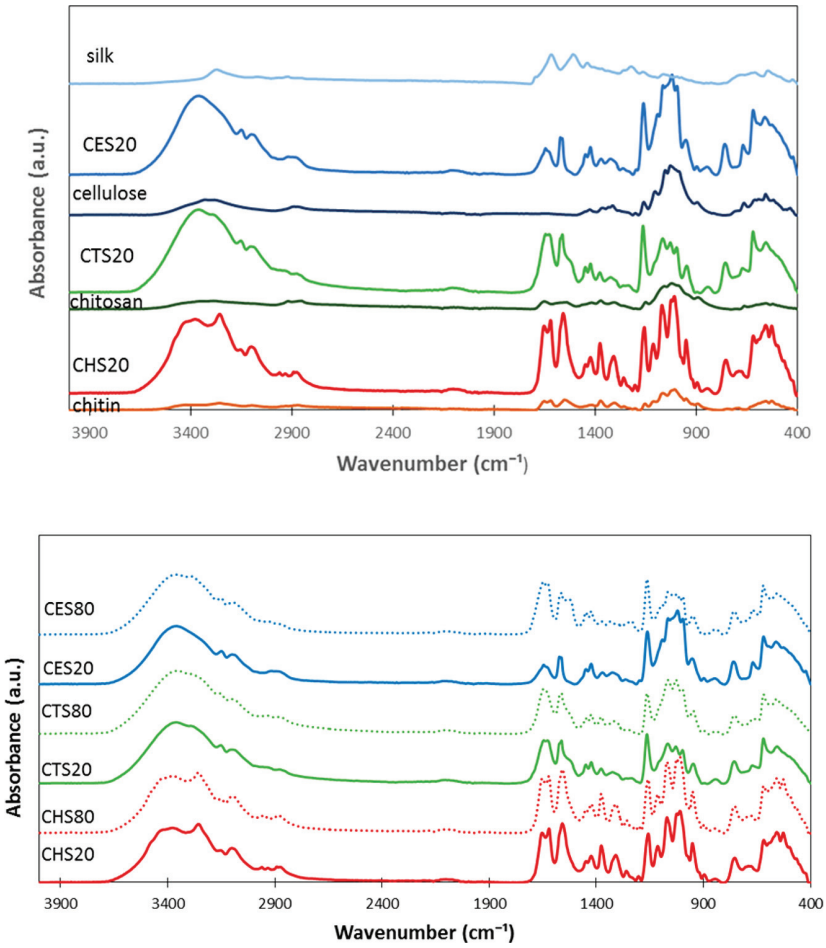

Figure 2. (top) Comparison of IR spectra for the pure polysaccharide chitin, chitosan cellulose, and protein silk, with spectra for the blended films chitin/silk 20 (CHS20), chitosan/silk 20 (CTS20), cellulose/silk 20 (CES20). (bottom) The IR spectra of 80% silk films cellulose/silk 80 (CES80), chitosan/silk 80 (CTS80), chitin/silk 80 (CHS80). CES20 and CHS20, CTS20 are reported in both graphs as a reference.

$$\epsilon_A = \epsilon_B = -\varepsilon \tag{13}$$

$$\epsilon_{AB} = -a\varepsilon \tag{14}$$

The reasoning here is that the only factor that matters is that ϵ_A and ϵ_B are bigger than ϵ_{AB}—their exact values are uninfluential. The factor a expresses ϵ_{AB} as a fraction of ε. Hence

$$\frac{N_A N_B}{N_{AB}^2} \approx \frac{1}{2} \exp\left(\frac{2\varepsilon - 2a\varepsilon}{k_B T}\right) \tag{15}$$

$$N_{AB}^2 \approx 2N_A N_B \exp\left(-\frac{2\varepsilon - 2a\varepsilon}{k_B T}\right) \tag{16}$$

Based on these values we can make the following predictions:

1. Even if $a = 0$, it is predicted that a few interfaces are formed. This is consistent with the formation of impurities even if the two materials are unlikely to blend.

2. As a increases, more and more interfaces are formed. As these interfaces have a lower cohesive energy than the A−A and B−B surfaces, it is expected that they are less stable as the temperature rises. Thus, it is expected that these interfaces will start decomposing at a lower temperature than the pure substance (see results in Thermal Analysis section and Table 3).

3. Since the formula is symmetric for concentrations of A and B, a material composed of 80% A and 20% B has the same number of interfaces as one composed of 80% B and 20% A. As a consequence, they will exhibit similar decomposition temperatures (see results in Thermal Analysis section and Table 3).

As a final remark, we notice that the model here proposed can be extended to consider more realistic cases, such as the fact that a layer may fold within the crystal and that some portion of the crystal may be unable to properly crystallize, presenting amorphous regions. We have included a more advanced model that accounts for these factors in the Supporting Information. This approach shows that the qualitative behavior described by eq 16 is respected.

RESULTS AND DISCUSSION

Structural Analysis. A first aspect to take into account for a proper comparison between our experiments and our theory is whether or not the two polymers were successfully mixed and interact at the molecular level. In other words, we aim to identify the presence of interfaces between the two polymers. Indeed, mixing takes place as can be evinced by analyzing the IR spectrum. Cellulose, chitin, chitosan, silk, and residual

DOI: 10.1021/acs.biomac.8b00903
Biomacromolecules 2018, 19, 3970−3982

AMIMCl have unique IR spectra (Figure 2). Common to all polysaccharides are the broad regions of OH (3500−3000 cm^{-1}) and C−O (around 1100 cm^{-1}). In addition, chitin and chitosan as well as silk show amide peaks at around 3200 and 1600 cm^{-1}.[80] The peaks at 1165 cm^{-1} are characteristic of residual AMIMCl.[81]

As shown from IR spectra in Figure 2, the blended films have more intense absorbance compared with the pure component, and there are some peaks (Amide I and II regions, 1576−1646 cm^{-1}) that appear in the cellulose/silk 20% (CES20) film, which did not appear in the pure cellulose spectra. This can be explained by the formation of new hydrogen bonds between the hydroxyl groups of cellulose and the amine groups in silk. Moreover, the spectra illustrate an increase in the absorbance of the Amide I and II regions (between 1576 and 1646 cm^{-1}) when 20% silk was added to all three polymers, as seen in Figure 2. In addition, a very intense Amide III peak (1260 cm^{-1}) appears in the chitin/silk 20% (CHS20) film, which may explain the extra strong hydrogen bonds found in chitin/silk mixtures.[47]

The amount of crystallinity can be evaluated using the IR spectrum.[61] At first, there seems to be no significant change in the IR spectra between 80% silk films and 20% silk films with the same polysaccharide (Figure 2). The major change is in the cellulose/silk 80% (CES80) film with the Amide I peak more intense than the Amide II peak. This trend is the opposite of what is observed for the 20% film (CES20). Overall, absorbance increases in the Amide (I, II) area as the mixture of silk with cellulose/chitin/chitosan increases from 20% to 80% silk as shown in Figure 2.

Even though the changes in the IR spectra may appear minimal, a calculation of the crystallinity (defined as the fraction of β-sheet content computed from the IR spectrum),[61] shows that the crystallinity increases with the addition of silk (Table 2). As can be seen from Table 2 the β-sheet content increases by 9.2% in cellulose/silk films, 19.8% in chitin/silk films, and 13.2% in chitosan-silk films. These trends are respected by our theoretical predictions, and we provide justification for these findings in the Dissolution and Regeneration section.

Table 2. Percentage of β-Sheet Crystallinity in Blended Films with 20% and 80% Silk, the Crystallinity Differences ($\Delta\phi$), and the Difference between Their First Decomposition Temperatures (ΔT) from Table 3

Polysaccharide	Crystallinity of β-sheet in 20% silk film	Crystallinity of β-sheet in 80% silk film	$\Delta\phi$	ΔT (°C)
Cellulose	28.4%	37.6%	9.2%	3
Chitin	22.4%	42.2%	19.8%	10
Chitosan	18.1%	31.3%	13.2%	7

Thermal Analysis. The model predicts that the number of interfaces should be the same for symmetric concentrations. Namely, in this study we have studied the 80%−20% and 20%−80% compositions. This leads to the following predictions (Figure 3):

1. The melting point is interpreted as the temperature at which the chains start separating from the crystal. In our model, the energy of separating the interface is lower than removing a chain from a pure substance. At this stage, it should be expected that residual solvent may play a role in lowering the melting point as solvent molecules trapped in the interfaces will act as defects, weakening the overall stability of the material.

2. After the interfaces start separating, chains in those interfaces will decompose. However, the chains within the pure blocks of material are still intact, leaving behind lingering crystalline regions. This is because within a crystal, part of the heat is stored in lattice vibrations, so the crystal as a whole may reach higher temperatures before it begins decomposing. This also explains why, generally, the melting of the polymer interfaces occurs before their decomposition (permitting they are not cross-linked).

3. As the temperature continues to grow, the small crystals of pure substance will begin to melt and then decompose in a manner similar to that described above. However, as the size of these crystals is much smaller than a typical macroscopic crystal of a pure substance, their melting/decomposition temperature is expected to be smaller than that of the pure material itself. This is a consequence of the Gibbs−Thomson formula that states that the melting/decomposition temperature T_m depends on the average width d_{avg} of crystal according to ref 82

$$T_m = T_m^0\left(1 - \frac{C}{d_{avg}}\right) \tag{17}$$

where C is a constant that depends on the material and T_m^0 is the melting temperature for a pure material ($d_{avg} \to \infty$).

4. A final prediction (that we could not test with our apparatus, but should be assessed in future studies) is related to the composition of the gases released during decomposition. As the first transition is associated with the decomposition of the interfaces, an analysis of the products should always reveal a 50%−50% mixture of molecules, no matter the actual composition of the blend as a whole. This is because the interface, by definition, is composed of one chain from each

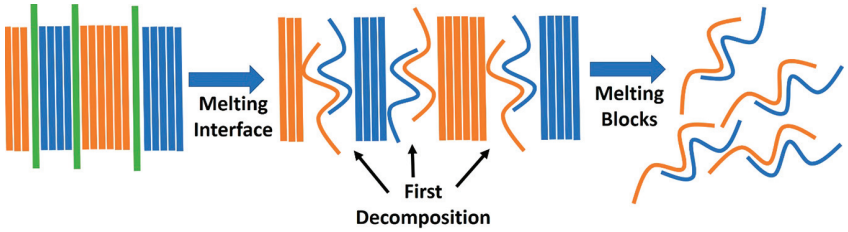

Figure 3. For a blend, the interfaces break down easily, so that a lot of small "pure" crystals are released. Immediately after melting, single chains are released from the interface and begin to decompose. The crystalline regions survive for a bit longer, before melting and decomposing in a similar way. Our model anticipates that this melting/decomposition will occur at a lower temperature than a perfect crystal.

DOI: 10.1021/acs.biomac.8b00903
Biomacromolecules 2018, 19, 3970−3982

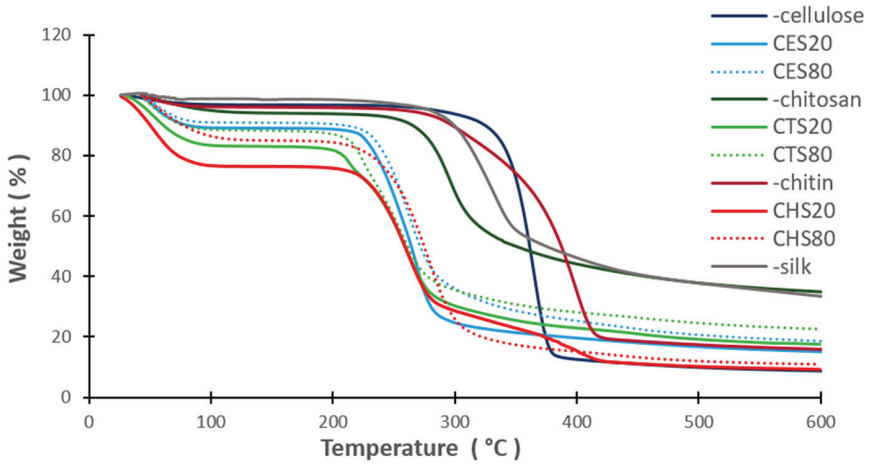

Figure 4. Thermal decomposition of the pure polysaccharides, silk, and blended films.

Table 3. Temperature of Highest Decomposition Rate

Sample	Temperature (°C)	Sample	Temperature (°C)	Sample	Temperature (°C)
Pure		20% silk		80% silk	
Cellulose	363	CES20	255, 268	CES80	258
Chitin	287, 396	CHS20	266, 386	CHS80	276
Chitosan	288	CTS20	217, 254	CTS80	224, 256
silk	322				

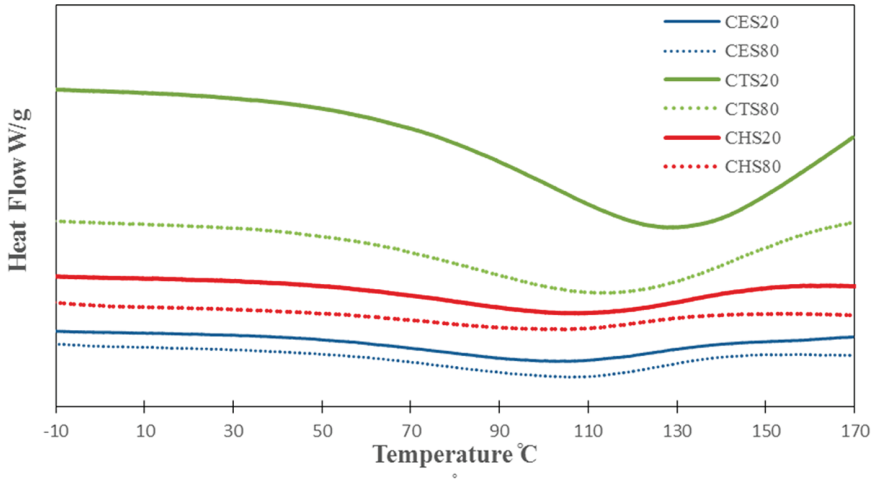

Figure 5. DSC curves of different silk−polysaccharide biocomposites presented in this study.

component of the binary polymer mixture. The second transition, of course, should reveal the actual composition of the sample as a whole.

These predictions (except for number 4) were validated via TGA analysis (Figure 4 and Table 3). The data are in excellent agreement with predictions 1−3.

From Table 3, it can be noted that films with a silk concentration of 20% all have two decomposition temperatures regardless of the type of polysaccharide, as anticipated by predictions 1 and 2 above (a two-step decomposition as shown in Figure 3 and 4). Notably, two 80% silk films (CES80 and CHS80) exhibit only one clear decomposition temperature. This may be due to a very small amount of mass being lost in one of the decomposition steps (making it difficult for our apparatus to detect) or the difference in temperatures between decomposition steps being extremely small when the polysaccharide content is low (20%). In accordance with prediction 3, decomposition of all blended films occurs at a much lower temperature than that of the pure material components. The maximum decomposition-rate temperature of the blended films also did not vary significantly according to the amount of silk, which is consistent with prediction 3 in the "stacking model" section (since 80%−20% and 20%−80% have a similar number of interfaces). As seen in Table 3, the maximum decomposition temperature only increases slightly when the amount of silk increases (20% to 80%) in all blended polysaccharides. The highest change in decomposition temperature is in chitin films (CHS20 to CHS80) with a ΔT of 10 °C, in accordance with the large increase in crystallinity revealed by our IR results (Table 2). The lowest change in temperature is in cellulose films (CES20 to CES80) with a ΔT of 3 °C, while chitosan films (CTS20 to CTS80) exhibit an

DOI: 10.1021/acs.biomac.8b00903
Biomacromolecules 2018, 19, 3970−3982

intermediate temperature change of ΔT = 7 °C (see Table 2 for a summary).

Glass Transition Temperature. For all biocomposites considered, the initial weight loss (below 100 °C), as shown in Figure 4, is due to the evaporation of residual water.[49,83] However, the glass transition temperature of the silk component is expected to be located in the same region.[42] Therefore, a more detailed analysis of this region is studied via DSC analysis (Figure 5). The DSC data are collected during a second DSC cycle scan as discussed in the Material and Methods section and thus, in practice, the free water molecules were removed during the first scan. As a consequence, the endothermic peaks are probably related to the glass transitions of the biocomposite blend-water system. Interestingly, the increased depth of the endothermic peaks is also correlated to a shift to a higher temperature. This is expected, as materials that retain bound water during the second cycle form stronger hydrogen bonds that require a higher temperature to be broken. In fact, as shown in Figure 5, chitosan does retain the largest amount of bound water, being able to coordinate more water molecules through its amine group.

Dissolution and Regeneration. Up until now, our model has assumed that the system is in thermal equilibrium with the surrounding environment. In this section, we will extend it to include kinetic effects, as well. In the previous section, we predicted that the first decomposition temperature should be the same for the 20%−80% and 80%−20% blend. While this prediction is largely respected, we previously noted that the 80%−20% decomposition temperatures are slightly higher than those in the 20%−80% case. In this section we want to present a detailed explanation for this behavior. To do so, we need to move one step back and discuss the dissolution process in more detail. We will start with the results of our simulations.

In order to investigate the dissolution process, we built a cellulose bilayer and we computed the free energy difference between fully associated and dissociated layers (as discussed in the Simulation Details in the Material and Methods section). As Figure 6 shows, the energy needed to separate entire layers

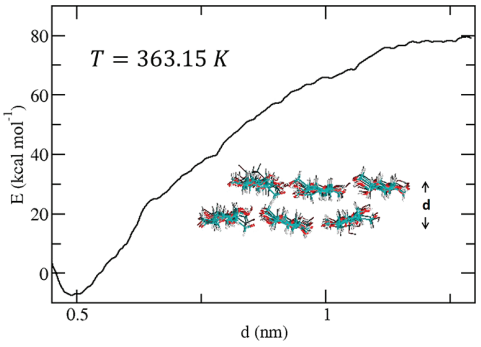

Figure 6. Free energy to separate two layers of pure cellulose.

is prohibitively large. On the other hand, separating one single chain from a layer by breaking the hydrogen bonds between them requires less energy (Figure 7) in agreement with observations from other simulations.[34,84] Therefore, while both dissolution mechanisms shown in Figures 6 and 7 are possible, it is overwhelmingly more likely for the process to occur via the separation mechanism shown in Figure 7. Movies showing the dissolution process for both cases is provided within the Supporting Information.

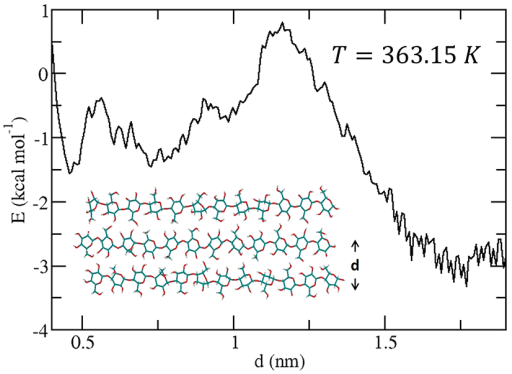

Figure 7. Free energy to separate one cellulose chain from an existing layer.

To generalize these results even further, we note that what really matters is how easily the hydrogen bonds between biopolymers can be broken in the dissolution process. While extensive simulations can, in principle, be performed to assess the stability of the hydrogen bonds between different biopolymers in different solvents, computationally it is extremely impractical to do so for every possible combination of biopolymer and solvent. However, a much more viable option in this case would be to extract the same amount of information by using a material's solubility in a particular solvent. While the solubility may not provide a molecular picture of the dissolution process, it is much more readily available in the literature for a wide variety of systems. We will now show that the solubility is a reliable parameter that can be used to predict the crystallinity of the final material.

The dissolution process of each biopolymer leads to a mixture of small crystalline regions and free chains (Figure 3). Under ideal conditions, the crystalline regions are expected to reach an equilibrium distribution with average thickness, d_{avg}. However, equilibrium conditions will not be reached during experimental time scales, thus we expect deviations from the average value d_{avg}. Therefore, during the regeneration process when we remove the ionic liquid, the crystals with size much smaller than d_{avg} will absorb free molecules and grow until they reach d_{avg}. On the other hand, if a crystal has an initial size much larger than d_{avg}, it will not dissolve within the time scale of the experiment. Finally, as eq 17 tells us, crystals with larger size will only disassemble (melt) at higher temperatures (or with higher energy provided).

Based on the discussion outline above, we can predict that

1. The molecule less soluble in the solvent will be more resistant to dissolution and will therefore lead to larger crystals. For our system,[85] this means that higher content of silk will lead to higher crystallinity, in agreement with Table 2.

2. If we define ΔT as the difference in the first decomposition temperature of a 20%−80% and an 80%−20% mixture, we expect that ΔT will be proportional to the difference in crystallinity $\Delta\phi$ between the respective mixtures. This is a consequence of point 1 (more crystallinity means larger pure blocks for the less soluble molecule) and eq 17 (larger pure blocks mean higher decomposition temperatures). In Table 3 we have compared these two quantities and this trend is respected.

3. The decomposition temperature of blended crystalline material is proportional to the solubility of the pure component materials in a certain solvent. The less a pure

DOI: 10.1021/acs.biomac.8b00903
Biomacromolecules 2018, 19, 3970−3982

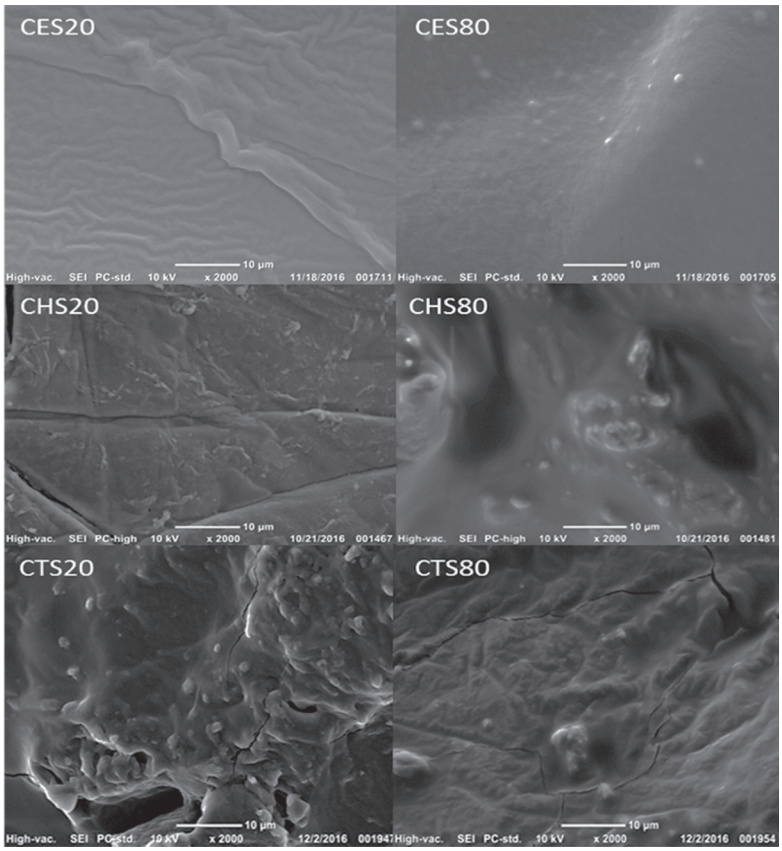

Figure 8. SEM images for polysaccharides/silk films at 20% and 80% silk (CES20), (CES80), (CHS20), (CHS80), (CTS20), and (CTS80).

material dissolves in the solvent, the smaller the ΔT between pure and composite material, ostensibly due to the decreased amount of interfaces formed during the mixing process. This hypothesis is supported by the results given in Table 3, where in our case, in the ionic liquid AMIMCl, the solubility of cellulose (up to 19% by weight)[86] > chitosan (about 5%)[87,88] > chitin (below 1%)[89,90] and ΔT between pure compounds and polysaccharide-silk blends follows a similar trend, i.e., cellulose > chitosan > chitin.

Morphology. By visual inspection, the observable morphology of the regenerated films differed according to the polysaccharide/protein composition: cellulose/silk films were characterized as firm and solid while chitin/silk and chitosan/silk films were brittle. To gain more insight into the morphology of the material we performed SEM imaging.

As can be seen in Figure 8 the SEM images demonstrate the topological changes in film morphology as the proportion of silk changes in the mixture with each polysaccharide. In general (Figure 8), the films with higher amounts of silk (80%) have smoother surfaces than films with less silk (20%), in agreement with other published work.[29] More specifically, cellulose films present a more fibrous structured surface (Figure 8, CES20) while chitosan films demonstrate a more porous surface (Figure 8, CTS20). Pores that can trap water in addition to the presence of the amide groups along the backbone of chitosan could explain the strong water retention from chitosan dominated materials, which can be confirmed by the initial water weight loss (below 100 °C) found in our TGA curves (Figure 4).[49,83]

Young's Modulus. The comparison between our model and our experiments suggests that crystalline regions of one molecular species are directly adjacent to structured or amorphous regions of another molecular species. Unfortunately, our model cannot currently describe the large-scale arrangement of the macromolecules at the level shown by the SEM topology. For instance, it cannot distinguish between lamellar-like structure and fiber-like structures. It is nevertheless interesting to compare our predictions with models that have been presented over the years to describe protein–polysaccharide blends. In a paper by Jin et al.,[47] the authors argue that silk fibroins are intercalated between the chitin molecular sheets in chitin–silk mixtures. We look to compare their measurement of the Young's modulus with that of the current theory. A detailed derivation is reported in the Supporting Information. In this approach, the Young's modulus E of a mixed material depends on its components according to

$$E = E_A(1 - x_s) + E_B x_s + \frac{E_A + E_B}{2}\sqrt{x_s(1 - x_s)}$$

where E_x is the Young's modulus of the pure component and x_s is the molar fraction of the added silk in the mixture. Interestingly, the final result only depends on the Young's modulus of the pure substances and does not rely on any fitting parameters. Using a silk–chitin blend system as an example, a comparison between the above theoretical prediction and the experimental results is reported in Figure 9, where the experimental data is obtained from Jin et al.[47]

DOI: 10.1021/acs.biomac.8b00903
Biomacromolecules 2018, 19, 3970–3982

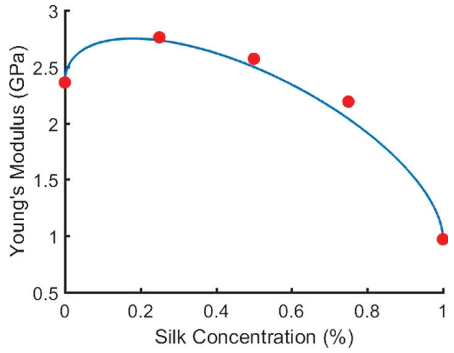

Figure 9. Young's modulus of silk−chitin biocomposites. The line represents the theoretical prediction in this study, while the points represent experimental data obtained from Jin et al.[47]

It is interesting to point out why the Young's modulus first increases sharply by adding a small amount of the second material (e.g., <20% of silk for the silk−chitin blend system), then gradually decreases with large amount of the second material. According to classical elasticity theory,[91] the elastic modulus of a material E is connected to its free-energy F

$$E = -\frac{\partial F}{\partial x}$$

where x is the direction over which the material is under stress. For a pure material, the entropy is negligible when compared to the energy of the system

$$E_{\text{pure}} = -\frac{\partial F}{\partial x} = -\frac{\partial U}{\partial x}$$

When a second component is added to the system, then the entropy appears. In addition, for small concentrations of the second component, we can assume that the energy does not change as the energy depends on the number of bonds between different molecules. As only a few interfaces are created, then it is expected that overall their effect on the energy is minimal. Hence

$$E_{\text{lowC}} = -\frac{\partial F}{\partial x} \approx -\frac{\partial U}{\partial x} + T\frac{\partial S}{\partial x} = E_{\text{pure}} + T\frac{\partial S}{\partial x}$$

Therefore, the Young's modulus is always expected to grow rapidly with the addition of a second component. As the entropy is a logarithmic function, it grows quickly for small amounts of the second component, but its growth rapidly stops for larger amounts. Beyond this point, the entropy is expected to become less important than the energetics, and the Young's modulus should start declining. As a concrete example, in the case of a 50:50 mixture the energetics of the system is dominant once again.

Proposed Mechanism. Based on the results presented above, we can summarize our findings and propose a pathway to the assembly of protein−polysaccharide materials (Figure 10). The first step consists of the dissolution of the original crystalline materials (in our case, polysaccharides and silk). The dissolution proceeds through the weakening of the extensive inter/intramolecular hydrogen bonding network of the crystalline materials as a consequence of the action of the solvent (ionic liquid). Studies have shown that, specifically, this occurs due to relatively strong interactions between the ionic liquid's anion and the hydrogen bond-accepting functional groups of the biopolymers.[92] While different solvents may lead to a different degree of dissolution, on the time scales associated with typical experiments, this process will always lead to a mixture of residual crystalline seeds and fully solvated chains. As discussed in the Dissolution and Regeneration section, this factor can be directly correlated to the thermal stability of the final blend. After the dissolution, water is added to wash out the ionic liquid. During this phase, the anions migrate from the biopolymer blend to the water. This notion can be argued based upon the almost complete absence of residual ionic liquid in the final blend as seen through IR (see Structural Analysis section). As the anions are essential to keeping the biomolecules separated as discussed above, the polymer chains start aggregating in their absence. However, the water rapidly replaces the anions which were once embedded in or next to the biopolymers, so that, at this point, there is competition between water molecules and other biopolymers to form hydrogen bonds. This leads to a phase separation with the formation of a hydrogel (biopolymer + water) and liquid phase (water + ionic liquid). It is interesting to note that this "gelation" process does not originate from a chemical cross-linking (the most common way of producing a hydrogel[93]) but from a competition between different interactions. The final step consists of the removal of the water and the formation of the intercalated protein−polysaccharide structure. As discussed in the Thermal Analysis section, the formation of this type of arrangement leads to well-defined features of the material's

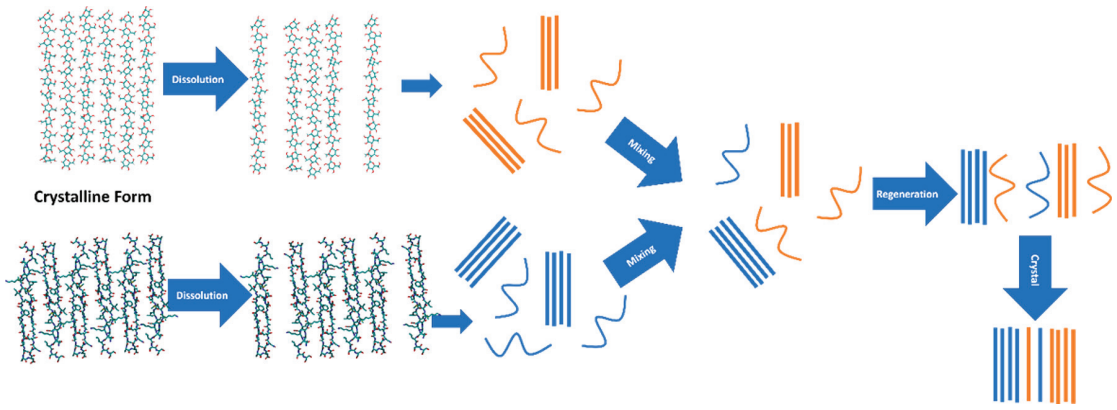

Figure 10. Schematic representation of the dissolution and regeneration process.

DOI: 10.1021/acs.biomac.8b00903
Biomacromolecules 2018, 19, 3970−3982

decomposition temperature that can be validated experimentally.

This simplified framework that involves all of the stages of the processing of the material just described can, in principle, be applied to other mixtures and used to predict the properties of the final blend. While not the primary focus of this paper, we want to point out that, in principle, the structure and properties of the material can be tuned at the level of the hydrogel, by using different solvents and alternative processing than that given here.[9,94−97] For instance, an important feature of many biopolymers, including the ones studied here, is the formation of β-sheets, which can be tuned with alcohol-based solvents.[40,97]

CONCLUSIONS

Here, we have combined theoretical modeling and molecular dynamics simulations in order to understand the dissolution and regeneration of biopolymer films. We have performed experiments in an effort to further investigate the process and compare our model's predictions of the properties of high and low concentrations of blended silk films using three different polysaccharides and the ionic liquid 1-allyl-3-methylimidazolium chloride (AMIMCl). We can conclude that silk can be used to fine-tune the properties of regenerated polysaccharide materials with respect to their β-sheet crystallinity, morphology, thermal stability, and Young's modulus. The theoretical model predicted the crystallinity and temperature trends successfully. From a theoretical point of view, our model and the experiments suggest that crystalline regions of one molecular species are directly adjacent to regions of another crystalline or amorphous molecular species. We have proven that this model correctly predicts the properties of the material as the polysaccharide-silk concentration is varied. In addition, we are now capable of describing the dissolution and regeneration process. This alone represents a major step in the advancement of biomaterial design.

ASSOCIATED CONTENT

Supporting Information

The Supporting Information is available free of charge on the ACS Publications website at DOI: 10.1021/acs.biomac.8b00903.

Figures describing the dissolution and decomposition process; more detailed derivation of the stacking model and Young's modulus (PDF)

Movie showing the dissolution process conducted using MD (MPG)

Movie showing the dissolution process conducted using MD (MPG)

AUTHOR INFORMATION

Corresponding Authors

*E-mail: david.salas@camden.rutgers.edu.

*E-mail: larini.camden@gmail.com.

ORCID

David Salas-de la Cruz: 0000-0002-5835-4325

Author Contributions

The manuscript was written through contributions of all authors. All authors have given approval to the final version of the manuscript. All authors contributed equally.

Notes

The authors declare no competing financial interest.

ACKNOWLEDGMENTS

We thank Shaun Tung and Anthony Cooper for useful discussions. Dr. Larini and Dr. Salas are supported by the start-up funds from Rutgers University-Camden. Dr. Salas and Dr. Hu are also supported by the National Science Foundation − DMR (grant no. 1809354 and 1809541). This work used the Extreme Science and Engineering Discovery Environment (XSEDE) (grant no. MCB150005 to L.L.), which is supported by National Science Foundation (grant no. ACI-1053575). Resources from the Texas Advanced Computing Center (TACC) and San Diego Supercomputing center (SDSC) were used as part of the XSEDE program. This study used the computational resources provided by the Center for Computational and Integrative Biology (CCIB) through the National Science Foundation (grant no. DBI-1126052). This research has been supported by RDI^2 through its ELF/Caliburn early adopter program. Amnah Hadadi was funded by the Saudi Arabian Cultural Mission (SACM).

REFERENCES

(1) Yin, J.; Luan, S. Opportunities and Challenges for the Development of Polymer-Based Biomaterials and Medical Devices. *Regener. Biomater.* **2016**, *3*, 129−135.

(2) Metzke, M.; Guan, Z. Structure-Property Studies on Carbohydrate-Derived Polymers for Use as Protein-Resistant Biomaterials. *Biomacromolecules* **2008**, *9*, 208−215.

(3) Kumar, S.; de A. e Silva, J.; Wani, M. Y.; Dias, C. M.; Sobral, A. J. Studies of Carbon Dioxide Capture on Porous Chitosan Derivative. *J. Dispersion Sci. Technol.* **2016**, *37*, 155−158.

(4) Zhang, X.; Wang, H.; Wen, X.; Zhang, A.; Wang, X.; Zhong, L.; Liu, C.; Sun, R. Synthesis and Characterization of Xylan Grafted with Polyethylene Glycol in Ionic Liquid and Their Use as Moisture-Absorption/Retention Biomaterials. *Macromol. Mater. Eng.* **2016**, *301*, 287−295.

(5) Mawad, D.; Lauto, A.; Wallace, G. G. In *Polymeric Hydrogels as Smart Biomaterials*; Springer: 2016; p 19−44.

(6) Wang, G.; He, Y.; Wang, H.; Zhang, L.; Yu, Q.; Peng, S.; Wu, X.; Ren, T.; Zeng, Z.; Xue, Q. A Cellulose Sponge with Robust Superhydrophilicity and under-Water Superoleophobicity for Highly Effective Oil/Water Separation. *Green Chem.* **2015**, *17*, 3093−3099.

(7) Ruiz-Palomero, C.; Soriano, M. L.; Valcárcel, M. Nanocellulose as Analyte and Analytical Tool: Opportunities and Challenges. *TrAC, Trends Anal. Chem.* **2017**, *87*, 1−18.

(8) Zhang, W.; Zhu, C.; Ye, D.; Xu, L.; Zhang, X.; Wu, Q.; Zhang, X.; Kaplan, D. L.; Jiang, X. Porous Silk Scaffolds for Delivery of Growth Factors and Stem Cells to Enhance Bone Regeneration. *PLoS One* **2014**, *9*, e102371.

(9) Kim, U.-J.; Park, J.; Joo Kim, H.; Wada, M.; Kaplan, D. L. Three-Dimensional Aqueous-Derived Biomaterial Scaffolds from Silk Fibroin. *Biomaterials* **2005**, *26*, 2775−2785.

(10) Zeng, S.; Liu, L.; Shi, Y.; Qiu, J.; Fang, W.; Rong, M.; Guo, Z.; Gao, W. Characterization of Silk Fibroin/Chitosan 3d Porous Scaffold and in Vitro Cytology. *PLoS One* **2015**, *10*, e0128658.

(11) Yucel, T.; Lovett, M. L.; Kaplan, D. L. Silk-Based Biomaterials for Sustained Drug Delivery. *J. Controlled Release* **2014**, *190*, 381−397.

(12) Takada, A.; Kadokawa, J.-i. Fabrication and Characterization of Polysaccharide Ion Gels with Ionic Liquids and Their Further Conversion into Value-Added Sustainable Materials. *Biomolecules* **2015**, *5*, 244−262.

(13) Kadokawa, J.-i.; Murakami, M.-a.; Takegawa, A.; Kaneko, Y. Preparation of Cellulose−Starch Composite Gel and Fibrous Material from a Mixture of the Polysaccharides in Ionic Liquid. *Carbohydr. Polym.* **2009**, *75*, 180−183.

DOI: 10.1021/acs.biomac.8b00903
Biomacromolecules 2018, 19, 3970−3982

(14) Singh, S.; Simmons, B. A.; Vogel, K. P. Visualization of Biomass Solubilization and Cellulose Regeneration During Ionic Liquid Pretreatment of Switchgrass. *Biotechnol. Bioeng.* **2009**, *104*, 68−75.
(15) Badgujar, K. C.; Bhanage, B. M. Factors Governing Dissolution Process of Lignocellulosic Biomass in Ionic Liquid: Current Status, Overview and Challenges. *Bioresour. Technol.* **2015**, *178*, 2−18.
(16) Stoddart, A.; Cleave, V. The Evolution of Biomaterials. *Nat. Mater.* **2009**, *8*, 444.
(17) Van Vlierberghe, S.; Dubruel, P.; Schacht, E. Biopolymer-Based Hydrogels as Scaffolds for Tissue Engineering Applications: A Review. *Biomacromolecules* **2011**, *12*, 1387−1408.
(18) Singh, N.; Rahatekar, S. S.; Koziol, K. K. K.; Ng, T. H. S.; Patil, A. J.; Mann, S.; Hollander, A. P.; Kafienah, W. Directing Chondrogenesis of Stem Cells with Specific Blends of Cellulose and Silk. *Biomacromolecules* **2013**, *14*, 1287−1298.
(19) Feng, Y.; Li, X.; Li, M.; Ye, D.; Zhang, Q.; You, R.; Xu, W. Facile Preparation of Biocompatible Silk Fibroin/Cellulose Nanocomposite Films with High Mechanical Performance. *ACS Sustainable Chem. Eng.* **2017**, *5*, 6227−6236.
(20) Guzman-Puyol, S.; Heredia-Guerrero, J. A.; Ceseracciu, L.; Hajiali, H.; Canale, C.; Scarpellini, A.; Cingolani, R.; Bayer, I. S.; Athanassiou, A.; Mele, E. Low-Cost and Effective Fabrication of Biocompatible Nanofibers from Silk and Cellulose-Rich Materials. *ACS Biomater. Sci. Eng.* **2016**, *2*, 526−534.
(21) Dong, X.; Zhao, Q.; Xiao, L.; Lu, Q.; Kaplan, D. L. Amorphous Silk Nanofiber Solutions for Fabricating Silk-Based Functional Materials. *Biomacromolecules* **2016**, *17*, 3000−3006.
(22) Boon, J. P.; Yip, S. *Molecular Hydrodynamics*; McGraw-Hill: New York, 1981.
(23) Flory, P. J. *Statistical Mechanics of Chain Molecules*; Wiley: New York, 1969.
(24) Flory, P. J. *Principles of Polymer Chemistry*; Cornell University Press: Ithaca, NY, 1953.
(25) Somendra, M. B.; Achille, G.; Amos, M. Flory Theory for Polymers. *J. Phys.: Condens. Matter* **2013**, *25*, 503101.
(26) de Gennes, P. G.; Prost, J. *The Physics of Liquid Crystals*; Oxford University Press: Oxford, 1995.
(27) Kadokawa, J.-I. Ionic Liquid as Useful Media for Dissolution, Derivatization, and Nanomaterial Processing of Chitin. *Green Sustainable Chem.* **2013**, *3*, 19−25.
(28) Xie, H.; Zhang, S.; Li, S. Chitin and Chitosan Dissolved in Ionic Liquids as Reversible Sorbents of Co2. *Green Chem.* **2006**, *8*, 630−633.
(29) Silva, S. S.; Santos, T. C.; Cerqueira, M. T.; Marques, A. P.; Reys, L. L.; Silva, T. H.; Caridade, S. G.; Mano, J. F.; Reis, R. L. The Use of Ionic Liquids in the Processing of Chitosan/Silk Hydrogels for Biomedical Applications. *Green Chem.* **2012**, *14*, 1463−1470.
(30) Jaworska, M. M.; Gorak, A. Modification of Chitin Particles with Chloride Ionic Liquids. *Mater. Lett.* **2016**, *164*, 341−343.
(31) Swatloski, R. P.; Spear, S. K.; Holbrey, J. D.; Rogers, R. D. Dissolution of Cellose with Ionic Liquids. *J. Am. Chem. Soc.* **2002**, *124*, 4974−4975.
(32) Isik, M.; Sardon, H.; Mecerreyes, D. Ionic Liquids and Cellulose: Dissolution, Chemical Modification and Preparation of New Cellulosic Materials. *Int. J. Mol. Sci.* **2014**, *15*, 11922.
(33) Gupta, K. M.; Jiang, J. Cellulose Dissolution and Regeneration in Ionic Liquids: A Computational Perspective. *Chem. Eng. Sci.* **2015**, *121*, 180−189.
(34) Rabideau, B. D.; Agarwal, A.; Ismail, A. E. Observed Mechanism for the Breakup of Small Bundles of Cellulose Iα and Iβ in Ionic Liquids from Molecular Dynamics Simulations. *J. Phys. Chem. B* **2013**, *117*, 3469−3479.
(35) Ghandi, K. A Review of Ionic Liquids, Their Limits and Applications. *Green Sustainable Chem.* **2014**, *04*, 44−53.
(36) Mallakpour, S.; Dinari, M. In *Green Solvents II*; Springer: 2012; pp 1−32.
(37) Chen, J.; Vongsanga, K.; Wang, X.; Byrne, N. What Happens During Natural Protein Fibre Dissolution in Ionic Liquids. *Materials* **2014**, *7*, 6158−6168.
(38) Stanton, J.; Xue, Y.; Pandher, P.; Malek, L.; Brown, T.; Hu, X.; Salas-de la Cruz, D. Impact of Ionic Liquid Type on the Structure, Morphology and Properties of Silk-Cellulose Biocomposite Materials. *Int. J. Biol. Macromol.* **2018**, *108*, 333−341.
(39) Stanton, J.; Xue, Y.; Waters, J. C.; Lewis, A.; Cowan, D.; Hu, X.; Salas-de la Cruz, D. Structure−Property Relationships of Blended Polysaccharide and Protein Biomaterials in Ionic Liquid. *Cellulose* **2017**, *4*, 1775−1789.
(40) DeFrates, K.; Markiewicz, T.; Callaway, K.; Xue, Y.; Stanton, J.; Salas de la Cruz, D.; Hu, X. Structure-Property Relationships of Thai Silk-Microcrystalline Cellulose Biocomposite Materials Fabricated from Ionic Liquid. *Int. J. Biol. Macromol.* **2017**, *104*, 919−928.
(41) Mohd, N.; Draman, S.; Salleh, M.; Yusof, N.; Mohd, N. Dissolution of Cellulose in Ionic Liquid: A Review. *AIP Conf. Proc.* **2016**, *1809*, 020035.
(42) Yazawa, K.; Ishida, K.; Masunaga, H.; Hikima, T.; Numata, K. Influence of Water Content on the B-Sheet Formation, Thermal Stability, Water Removal, and Mechanical Properties of Silk Materials. *Biomacromolecules* **2016**, *17*, 1057−1066.
(43) García Mir, V.; Heinämäki, J.; Antikainen, O.; Iraizoz Colarte, A.; Airaksinen, S.; Karjalainen, M.; Bilbao Revoredo, O.; Nieto, O. M.; Yliruusi, J. Effects of Moisture on Tablet Compression of Chitin. *Carbohydr. Polym.* **2011**, *86*, 477−483.
(44) Viljoen, J. M.; Steenekamp, J. H.; Marais, A. F.; Kotzé, A. F. Effect of Moisture Content, Temperature and Exposure Time on the Physical Stability of Chitosan Powder and Tablets. *Drug Dev. Ind. Pharm.* **2014**, *40*, 730−742.
(45) Mokhothu, T. H.; John, M. J. Review on Hygroscopic Aging of Cellulose Fibres and Their Biocomposites. *Carbohydr. Polym.* **2015**, *131*, 337−354.
(46) Rabotyagova, O. S.; Cebe, P.; Kaplan, D. L. Protein-Based Block Copolymers. *Biomacromolecules* **2011**, *12*, 269−289.
(47) Jin, J.; Hassanzadeh, P.; Perotto, G.; Sun, W.; Brenckle, M. A.; Kaplan, D.; Omenetto, F. G.; Rolandi, M. A Biomimetic Composite from Solution Self-Assembly of Chitin Nanofibers in a Silk Fibroin Matrix. *Adv. Mater.* **2013**, *25*, 4482−4487.
(48) Sharma, C.; Dinda, A. K.; Potdar, P. D.; Mishra, N. C. Fabrication of Quaternary Composite Scaffold from Silk Fibroin, Chitosan, Gelatin, and Alginate for Skin Regeneration. *J. Appl. Polym. Sci.* **2015**, *132*, 1−12.
(49) Fernandes, L. L.; Resende, C. X.; Tavares, D. S.; Soares, G. A.; Castro, L. O.; Granjeiro, J. M. Cytocompatibility of Chitosan and Collagen-Chitosan Scaffolds for Tissue Engineering. *Polim.: Cienc. Tecnol.* **2011**, *21*, 1−6.
(50) Chen, L.; Zhou, M.-L.; Qian, Z.-G.; Kaplan, D. L.; Xia, X.-X. Fabrication of Protein Films from Genetically Engineered Silk-Elastin-Like Proteins by Controlled Cross-Linking. *ACS Biomater. Sci. Eng.* **2017**, *3*, 335−341.
(51) Rajkhowa, R.; Hu, X.; Tsuzuki, T.; Kaplan, D. L.; Wang, X. Structure and Biodegradation Mechanism of Milled Bombyx Mori Silk Particles. *Biomacromolecules* **2012**, *13*, 2503−2512.
(52) Guo, C.; Zhang, J.; Jordan, J. S.; Wang, X.; Henning, R. W.; Yarger, J. L. Structural Comparison of Various Silkworm Silks: An Insight into the Structure−Property Relationship. *Biomacromolecules* **2018**, *19*, 906−917.
(53) Marsano, E.; Corsini, P.; Canetti, M.; Freddi, G. Regenerated Cellulose-Silk Fibroin Blends Fibers. *Int. J. Biol. Macromol.* **2008**, *43*, 106−114.
(54) Tian, D.; Li, T.; Zhang, R.; Wu, Q.; Chen, T.; Sun, P.; Ramamoorthy, A. Conformations and Intermolecular Interactions in Cellulose/Silk Fibroin Blend Films: A Solid-State Nmr Perspective. *J. Phys. Chem. B* **2017**, *121*, 6108−6116.
(55) Bhardwaj, N.; Kundu, S. C. Silk Fibroin Protein and Chitosan Polyelectrolyte Complex Porous Scaffolds for Tissue Engineering Applications. *Carbohydr. Polym.* **2011**, *85*, 325−333.
(56) Huang, S.-C.; Qian, Z.-G.; Dan, A.-H.; Hu, X.; Zhou, M.-L.; Xia, X.-X. Rational Design and Hierarchical Assembly of a Genetically Engineered Resilin−Silk Copolymer Results in Stiff Hydrogels. *ACS Biomater. Sci. Eng.* **2017**, *3*, 1576−1585.

DOI: 10.1021/acs.biomac.8b00903
Biomacromolecules 2018, 19, 3970−3982

(57) Xia, X.-X.; Xu, Q.; Hu, X.; Qin, G.; Kaplan, D. L. Tunable Self-Assembly of Genetically Engineered Silk−Elastin-Like Protein Polymers. *Biomacromolecules* **2011**, *12*, 3844−3850.
(58) Kadokawa, J.-i.; Takegawa, A.; Mine, S.; Prasad, K. Preparation of Chitin Nanowhiskers Using an Ionic Liquid and Their Composite Materials with Poly(Vinyl Alcohol). *Carbohydr. Polym.* **2011**, *84*, 1408−1412.
(59) Prasad, K.; Murakami, M.-a.; Kaneko, Y.; Takada, A.; Nakamura, Y.; Kadokawa, J.-i. Weak Gel of Chitin with Ionic Liquid, 1-Allyl-3-Methylimidazolium Bromide. *Int. J. Biol. Macromol.* **2009**, *45*, 221−225.
(60) Youngs, T. G. A.; Hardacre, C.; Holbrey, J. D. Glucose Solvation by the Ionic Liquid 1,3-Dimethylimidazolium Chloride: A Simulation Study. *J. Phys. Chem. B* **2007**, *111*, 13765−13774.
(61) Hu, X.; Kaplan, D.; Cebe, P. Determining Beta-Sheet Crystallinity in Fibrous Proteins by Thermal Analysis and Infrared Spectroscopy. *Macromolecules* **2006**, *39*, 6161−6170.
(62) Woods Group Complex Carbohydrate Research Center; University of Georgia, Athens, GA, 2005−2017.
(63) Humphrey, W.; Dalke, A.; Schulten, K. Vmd: Visual Molecular Dynamics. *J. Mol. Graphics* **1996**, *14*, 33−38.
(64) Wang, J.; Wang, W.; Kollman, P. A.; Case, D. A. Automatic Atom Type and Bond Type Perception in Molecular Mechanical Calculations. *J. Mol. Graphics Modell.* **2006**, *25*, 247−260.
(65) Wang, J.; Wolf, R. M.; Caldwell, J. W.; Kollman, P. A.; Case, D. A. Development and Testing of a General Amber Force Field. *J. Comput. Chem.* **2004**, *25*, 1157−1174.
(66) Abraham, M. J.; Murtola, T.; Schulz, R.; Páll, S.; Smith, J. C.; Hess, B.; Lindahl, E. Gromacs: High Performance Molecular Simulations through Multi-Level Parallelism from Laptops to Supercomputers. *SoftwareX* **2015**, *1−2*, 19−25.
(67) Berendsen, H. J. C.; van der Spoel, D.; van Drunen, R. Gromacs: A Message-Passing Parallel Molecular Dynamics Implementation. *Comput. Phys. Commun.* **1995**, *91*, 43−56.
(68) Hess, B.; Kutzner, C.; van der Spoel, D.; Lindahl, E. Gromacs 4: Algorithms for Highly Efficient, Load-Balanced, and Scalable Molecular Simulations. *J. Chem. Theory Comput.* **2008**, *4*, 435−447.
(69) Lindahl, E.; Hess, B.; van der Spoel, D. Gromacs 3.0: A Package for Molecular Simulation and Trajectory Analysis. *J. Mol. Model.* **2001**, *7*, 306−317.
(70) Páll, S.; Abraham, M. J.; Kutzner, C.; Hess, B.; Lindahl, E. In *Solving Software Challenges for Exascale: International Conference on Exascale Applications and Software, Easc 2014, Stockholm, Sweden, April 2−3, 2014, Revised Selected Papers*, Markidis, S.; Laure, E., Eds.; Springer International Publishing: Cham, 2015; pp 3−27.
(71) Pronk, S.; Páll, S.; Schulz, R.; Larsson, P.; Bjelkmar, P.; Apostolov, R.; Shirts, M. R.; Smith, J. C.; Kasson, P. M.; van der Spoel, D.; et al. Gromacs 4.5: A High-Throughput and Highly Parallel Open Source Molecular Simulation Toolkit. *Bioinformatics* **2013**, *29*, 845−854.
(72) van der Spoel, D.; Lindahl, E.; Hess, B.; Groenhof, G.; Mark, A. E.; Berendsen, H. J. C. Gromacs: Fast, Flexible and Free. *J. Comput. Chem.* **2005**, *26*, 1701−1719.
(73) Kirschner, K. N.; Yongye, A. B.; Tschampel, S. M.; González-Outeiriño, J.; Daniels, C. R.; Foley, B. L.; Woods, R. J. Glycam06: A Generalizable Biomolecular Force Field. Carbohydrates. *J. Comput. Chem.* **2008**, *29*, 622−655.
(74) Darden, T.; York, D.; Pedersen, L. Particle Mesh Ewald: An N • Log(N) Method for Ewald Sums in Large Systems. *J. Chem. Phys.* **1993**, *98*, 10089−10092.
(75) Essmann, U.; Perera, L.; Berkowitz, M. L.; Darden, T.; Lee, H.; Pedersen, L. G. A Smooth Particle Mesh Ewald Method. *J. Chem. Phys.* **1995**, *103*, 8577−8593.
(76) Berendsen, H. J. C.; Postma, J. P. M.; van Gunsteren, W. F.; DiNola, A.; Haak, J. R. Molecular Dynamics with Coupling to an External Bath. *J. Chem. Phys.* **1984**, *81*, 3684−3690.
(77) Hoover, W. G. Canonical Dynamics: Equilibrium Phase-Space Distributions. *Phys. Rev. A: At., Mol., Opt. Phys.* **1985**, *31*, 1695−1697.
(78) Nosé, S. A Molecular Dynamics Method for Simulations in the Canonical Ensemble. *Mol. Phys.* **1984**, *52*, 255−268.
(79) Kumar, S.; Rosenberg, J. M.; Bouzida, D.; Swendsen, R. H.; Kollman, P. A. The Weighted Histogram Analysis Method for Free-Energy Calculations on Biomolecules. I. The Method. *J. Comput. Chem.* **1992**, *13*, 1011−1021.
(80) Kumirska, J.; Czerwicka, M.; Kaczyński, Z.; Bychowska, A.; Brzozowski, K.; Thöming, J.; Stepnowski, P. Application of Spectroscopic Methods for Structural Analysis of Chitin and Chitosan. *Mar. Drugs* **2010**, *8*, 1567−1636.
(81) Kathirgamanathan, K.; Grigsby, W. J.; Al-Hakkak, J.; Edmonds, N. R. Two-Dimensional Ftir as a Tool to Study the Chemical Interactions within Cellulose-Ionic Liquid Solutions. *Int. J. Polym. Sci.* **2015**, *2015*, 1−9.
(82) Crist, B. Equilibrium Aspects of Folded Chain Polymer Crystals. *Macromolecules* **2006**, *39*, 1971−1980.
(83) Teimouri, A.; Azadi, M. Preparation and Characterization of Novel Chitosan/Nanodiopside/Nanohydroxyapatite Composite Scaffolds for Tissue Engineering Applications. *Int. J. Polym. Mater.* **2016**, *65*, 917−927.
(84) Li, Y.; Liu, X.; Zhang, S.; Yao, Y.; Yao, X.; Xu, J.; Lu, X. Dissolving Process of a Cellulose Bunch in Ionic Liquids: A Molecular Dynamics Study. *Phys. Chem. Chem. Phys.* **2015**, *17*, 17894−17905.
(85) Phillips, D. M.; Drummy, L. F.; Conrady, D. G.; Fox, D. M.; Naik, R. R.; Stone, M. O.; Trulove, P. C.; De Long, H. C.; Mantz, R. A. Dissolution and Regeneration of Bombyx Mori Silk Fibroin Using Ionic Liquids. *J. Am. Chem. Soc.* **2004**, *126*, 14350−14351.
(86) Xing, L.; Wu, Z.; Gong, G. Dissolution of Cotton Cellulose with Ionic Liquids 1-Butyl-3-Methylimidazolium Chloride and 1-Allyl-3-Methylimidazolium Chloride to Prepare Reducing Sugar. *J. Energy Eng.* **2014**, *140*, 04013013.
(87) Liu, L.; Zhou, S.; Wang, B.; Xu, F.; Sun, R. Homogeneous Acetylation of Chitosan in Ionic Liquids. *J. Appl. Polym. Sci.* **2013**, *129*, 28−35.
(88) Xiao, W.; Chen, Q.; Wu, Y.; Wu, T.; Dai, L. Dissolution and Blending of Chitosan Using 1,3-Dimethylimidazolium Chloride and 1-H-3-Methylimidazolium Chloride Binary Ionic Liquid Solvent. *Carbohydr. Polym.* **2011**, *83*, 233−238.
(89) Wang, W.-T.; Zhu, J.; Wang, X.-L.; Huang, Y.; Wang, Y.-Z. Dissolution Behavior of Chitin in Ionic Liquids. *J. Macromol. Sci., Part B: Phys.* **2010**, *49*, 528−541.
(90) Chen, X.; Liu, Y.; Kerton, F. M.; Yan, N. Conversion of Chitin and N-Acetyl-D-Glucosamine into a N-Containing Furan Derivative in Ionic Liquids. *RSC Adv.* **2015**, *5*, 20073−20080.
(91) Strobl, G. *The Physics of Polymers*; Springer Verlag: New York, 2007.
(92) Mohd, N.; Draman, S. F. S.; Salleh, M. S. N.; Yusof, N. B. Dissolution of Cellulose in Ionic Liquid. *AIP Conf. Proc.* **2016**, *1809*, 020035.
(93) Ahmed, E. M. Hydrogel: Preparation, Characterization, and Applications: A Review. *J. Adv. Res.* **2015**, *6*, 105−121.
(94) Shang, S.; Zhu, L.; Fan, J. Intermolecular Interactions between Natural Polysaccharides and Silk Fibroin Protein. *Carbohydr. Polym.* **2013**, *93*, 561−573.
(95) Mukuze, K. S.; Yao, Y.; Xia, X.; Zhang, Y. Effect of Coagulation Agents on Morphology and Structure of Cellulose/Silk Fibroin Films with 1-Butyl-3-Ethylimidazolium Chloride as Solvent. *Mater. Res. Innovations* **2014**, *18*, S4.
(96) Liu, L.; Yang, X.; Yu, H.; Ma, C.; Yao, J. Biomimicking the Structure of Silk Fibers Via Cellulose Nanocrystal as [Small Beta]-Sheet Crystallite. *RSC Adv.* **2014**, *4*, 14304−14313.
(97) Jin, H. J.; Park, J.; Karageorgiou, V.; Kim, U. J.; Valluzzi, R.; Cebe, P.; Kaplan, D. L. Water-Stable Silk Films with Reduced B-Sheet Content. *Adv. Funct. Mater.* **2005**, *15*, 1241−1247.

DOI: 10.1021/acs.biomac.8b00903
Biomacromolecules 2018, 19, 3970−3982